https://doi.org/10.1007/s41230-026-5126-1

Effect of modification treatment on microstructure and properties of Fe-B-C alloy

Li-qiong Zhong[1], Qiang Xiao[2], Feng-shuo Jin[3, 4], **Wei-ji Lai[5], and *Yan-liang Yi[3, 4]

1. School of Mechanical Engineering, Guiyang University, Guiyang 550005, China

2. Department of Titanium Metal Research, Chengdu Institute of Advanced Metallic Material Technology and Industry Co., Ltd., Chengdu 610305, China

3. Institute of Advance Wear & Corrosion Resistant and Functional Materials, Jinan University, Guangzhou 510632, China

4. Shaoguan Research Institute of Jinan University, Shaoguan 512027, Guangdong, China

5. Sinomach Heavy Equipment Group Co., Ltd., Deyang 618000, Sichuan, China

Abstract: The network structure of M_2B in Fe-B-C alloy readily leads to the failure of material. In this work, by adding K_2SO_4, the morphology of the M_2B was successfully regulated through a synergistic treatment combining active element modification and heterogeneous nucleation modification. The results show that after the addition of K_2SO_4, a new phase α-MnS forms in the alloy, and the active element K enriches at the M_2B/matrix interface. This inhibits the growth of the network M_2B and promotes its transformation from a continuous network structure to an isolated blocky structure. As the K_2SO_4 addition increases from 0wt.% to 4.46wt.%, the shape factor value of M_2B increases from 0.067 to 0.353, with an increase of 426%. The impact toughness of the alloy increases from 5.9 $J·cm^{-2}$ to 14.2 $J·cm^{-2}$, and the fracture mode transitions from cleavage fracture to ductile-cleavage mixed fracture. Three-body abrasion tests indicate that with increasing K_2SO_4 addition, the wear weight loss of the alloy gradually decreases. The alloy with 4.46wt.% K_2SO_4 addition exhibits the least wear damage and the best wear resistance. This work provides an effective approach for regulating the microstructure and improving the wear resistance of wear-resistant Fe-B-C alloys.

Keywords: Fe-B-C alloy; borides; modification; three-body abrasion

CLC numbers: TG142.72 **Document code:** A **Article ID:** 1672-6421(2026)02-215-08

1 Introduction

The application of Fe-B-C alloy in wear-resistant fields is continually expanding, notably in mining machinery, automotive components, and tool manufacturing. In mining machinery, the superior wear resistance of Fe-B-C alloy significantly extends equipment service life and reduces maintenance costs[1]. For automotive components, the high wear resistance of Fe-B-C alloy improves the durability of critical parts such as engine components and braking systems, thereby enhancing overall vehicle performance[2]. In tool manufacturing, the low cost, high performance, and long service life characteristics of Fe-B-C alloy substantially advance technological progress in this sector[3]. The development of Fe-B-C alloy not only meets the industrial demand for high-performance wear-resistant materials but also offers significant economic advantages, making it highly valuable for advancing manufacturing sector and economic efficiency.

In Fe-B-C alloy, the hard phase M_2B solidifies via a non-faceted-faceted eutectic reaction, exhibiting strong anisotropy[4]. Its solid-liquid interface comprises specific crystallographic planes, typically resulting in a coarse, continuous network structure upon solidification[5, 6]. This structure is prone to stress concentration and can cause rapid crack propagation along the network under stress, leading to material failure[7, 8]. Modification treatment is the most common method for optimizing the phase morphology and improving the properties of alloys, which mainly

*Yan-liang Yi

Male, born in 1989, Ph. D., Associate Professor. Research interests: Advanced metal preparation and processing. His academic research has led to the publication of more than 70 technical papers.

E-mail: y_yanliang@163.com

**Wei-ji Lai

E-mail: lwj9279@163.com

Received: 2025-06-06; Revised: 2025-08-20; Accepted: 2025-11-03

consists of active element modification and heterogeneous nucleation modification. Common active elements include Group I and II elements[9, 10] and rare earth[11, 12], which primarily act on the solid-liquid interface to modify the phase growth behavior during solidification. Heterogeneous nucleation increases the number of effective heterogeneous nuclei within the alloy, enhancing the nucleation rate and ultimately enabling control over microstructure morphology and grain refinement.

Building on this, by adding K_2SO_4 to the research alloy, the present work realized a synergistic modification treatment combining active element adsorption and heterogeneous nucleation for M_2B phase morphology regulation. Through this morphology control, an advanced wear-resistant Fe-B-C alloy with high performance, and long service life was developed.

2 Experimental materials and methods

2.1 Material preparation

The nominal composition of the alloy is 0.36 C, 2.00 B, 2.50 Cr, 1.81 Mn, 1.24 Ni, 1.50 Si, and 90.59 Fe (wt.%). K_2SO_4 was added to introduce the active element K and heterogeneous nucleation (α-MnS). Samples were designated K0, K0.4, K0.8, K1.2, K1.6, and K2 based on the nominal K addition amount, with the corresponding chemical compositions listed in Table 1. Raw materials were melted in a 10 kg medium-frequency induction furnace. The molten metal was poured into a ladle containing 5 mm diameter K_2SO_4 particles, then cast into Y-shaped silica sand molds preheated to approximately 1,400 °C. Samples were subsequently sectioned from the cast ingot into 10 cm×10 cm×10 cm cubes, heat-treated at 1,000 °C for 1 h followed by natural cooling, and then tempered at 220 °C for 2 h.

Table 1: Nominal chemical composition of Fe-B-C alloys (wt.%)

Sample	Element content							Nominal K addition	K_2SO_4 addition
	C	B	Mn	Ni	Si	Cr	Fe		
K0	0.36	2.00	1.81	1.24	1.50	2.50	Bal.	0.00	0.00
K0.4								0.40	0.89
K0.8								0.80	1.78
K1.2								1.20	2.68
K1.6								1.60	3.57
K2								2.00	4.46

2.2 Material characterization

After heat treatment, the samples were sectioned, sequentially ground using #400, #800, #1200, #1600, and #2000 abrasive papers, polished with 5 μm diamond paste, and etched with 4% nital solution. Phase identification was performed using a Rigaku D/Max-2400X diffractometer operated at 40 kV and 200 mA, scanning from 15° to 90° at 5°·min^{-1}. Microstructural characterization was conducted using scanning electron microscopy (SEM, JSM-6510A) and electron probe microanalysis (EPMA, JXA-iSP100).

Macrohardness was measured using an MX1000 microhardness tester under a 50 N load, with results averaged over five tests. Impact toughness testing was performed at room temperature using a pendulum impact tester according to ASTM E23-18. Unnotched samples (10 mm×10 mm×55 mm) were used for the tests, with results averaged over three trials.

Three-body abrasion tests were conducted using a custom-built block-on-ring geometry tester based on the Boyes design[13], with the schematic diagram shown in Fig. 1. WC particles (#180 grit size) served as the abrasive. During wear testing, the sample rotated along a circular track, while the abrasive flowed between the sample and the wear ring. The test parameters were: rotation speed of 30 rpm for 30 min under normal loads of 50, 70, and 90 N. Subsequently, the samples were ultrasonically cleaned for 5 min, and then weighed using a precision balance with an accuracy of 1×10^{-4} g. The weight losses were averaged over three tests. The wear track morphology was characterized using a 3D laser scanning microscope (VK-X200K) and SEM.

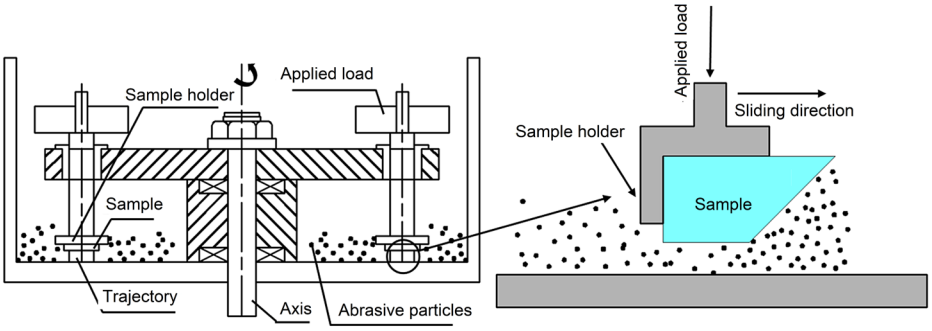

Fig. 1: Schematic diagram of three-body abrasion tester

3 Results and discussion

3.1 Microstructure

Figure 2 shows XRD patterns of samples with varying K_2SO_4 addition amounts. The K0 sample consists of α-Fe, M_2B, and $M_{23}(B,C)_6$ phases. After adding K_2SO_4 (taking K0.8 and K2 samples as examples), a new α-MnS phase is formed. This is attributed to the low solute equilibrium partition coefficient and low solubility of S in the alloy, which promotes the precipitation of sulfides (e.g., FeS) in the molten metal. The affinity of S for different metallic elements governs the type of sulfide formed, with the formation sequence being: CeS>CaS>Zr_3S_4>TiS>MgS>MnS>FeS[14]. Consequently, the addition of K_2SO_4 enables S to combine with existing Mn to form α-MnS. This α-MnS can serve as a heterogeneous nucleation core for the M_2B phase. The lattice misfit between α-MnS and M_2B on major crystal planes such as (100) and (110) is only 1.94%–2.16%[15], which is much lower than the critical value of 15%, indicating that the α-MnS can promote the heterogeneous nucleation of M_2B.

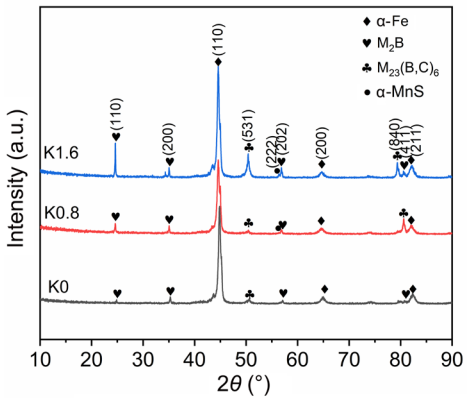

Fig. 2: XRD patterns of Fe-B-C alloys with different K_2SO_4 additions

SEM micrographs of samples with different K_2SO_4 additions are presented in Fig. 3. For the sample without K_2SO_4 addition (i.e., K0), as can be seen from Fig. 3(a), the M_2B phase primarily exhibits a network, fishbone-like, or clustered structure. When 0.89wt.% K_2SO_4 is added (i.e., K0.4), the amount of network M_2B structure decreases, and the α-MnS can be observed (marked by circle), as shown in Fig. 3(b). With the addition of 1.78wt.% K_2SO_4 [i.e., K0.8, as shown in Fig. 3(c)], the M_2B network structure significantly diminishes, showing signs of spheroidization. At a K_2SO_4 addition of 2.68wt.% [Fig. 3(d)], the M_2B morphology in K1.2 changes drastically, transitioning from network to a rod-like structure. With the addition of 4.46wt.% K_2SO_4 (i.e., K2), the M_2B phase transforms into isolated rod-like or block-like structures, as shown in Fig. 3(f). Overall, K_2SO_4 addition markedly improves the M_2B morphology in the Fe-B-C alloy. In addition, the matrix of samples with different K_2SO_4 additions is entirely martensite, containing fine and dispersed $M_{23}(B,C)_6$ secondary precipitates.

EPMA point scanning analysis was performed on the main phases of the alloy in Fig. 3, and the results are shown in Fig. 4. It can be seen that S and Mn exhibit a synergistic enrichment characteristic and form a black circular phase, as shown in the enlarged microstructure in Fig. 3(f). In this phase, the mass fraction of S is 33.33%, and that of Mn is 66.67%. Based on calculations using the atomic weights of the elements, the atomic ratio of S to Mn in this phase is close to 1:1. This is consistent with theoretical atomic formula of the α-MnS phase. For the M_2B phase, B, C, Fe, Cr, and Mn are all distributed in this phase, with mass fractions of 17.96%, 13.87%, 56.49%, 7.34%, and 4.34%, respectively. The atomic ratio of each element is approximately B:21.0, C:14.6, Fe:12.8, Cr:1.8, Mn:1.0, which conforms to the structural characteristics of M_2B-type borides (where "M" represents multiple transition metal elements). It can be found from the

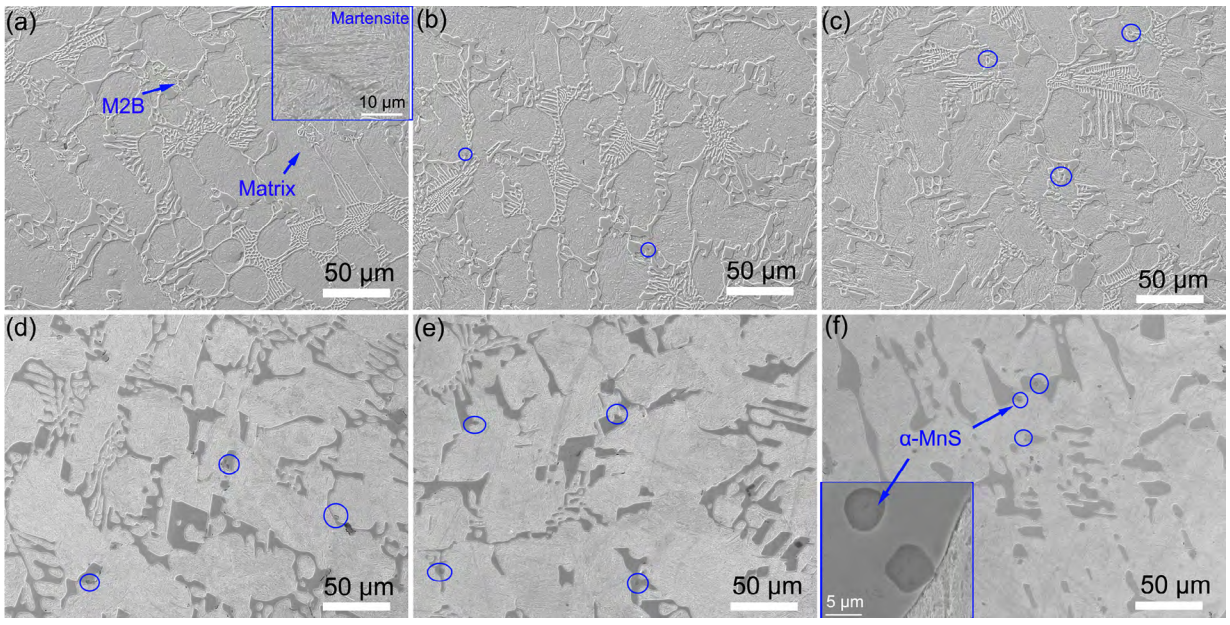

Fig. 3: SEM micrographs of Fe-B-C alloys with different K_2SO_4 additions: (a) K0; (b) K0.4; (c) K0.8; (d) K1.2; (e) K1.6; (f) K2

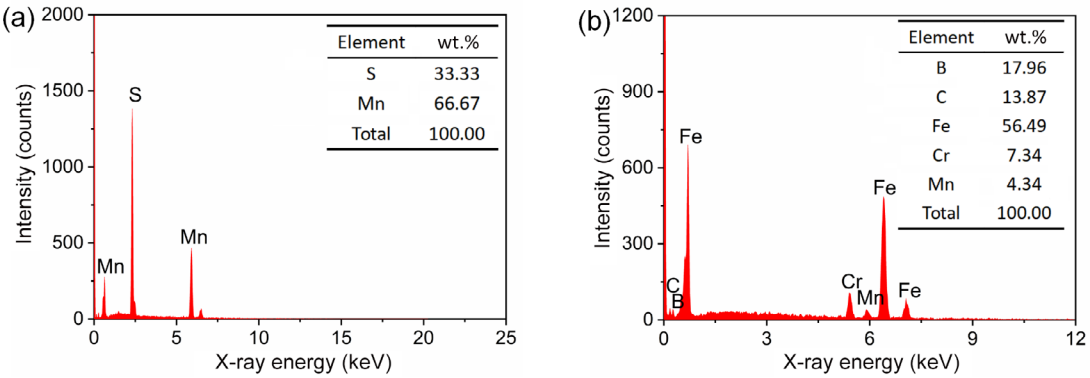

Fig. 4: EPMA point scanning results of different phases: (a) α-MnS; (b) M_2B

enlarged microtructure in Fig. 3(f) that the M_2B is mainly encapsulated within the epitaxial growth region of α-MnS. This growth behavior indirectly confirms that α-MnS can serve as a heterogeneous core for the M_2B, thereby improving the structural morphology of M_2B.

To quantify the modification effect, the shape factor (f) of the M_2B borides was measured. Twenty SEM images (500x magnification) for each sample were processed using Photoshop to color M_2B green and α-MnS red, as shown in Fig. 5(a). Image-Pro Plus 6.0 software was then used to measure the perimeter (L) and area (A) of the colored M_2B regions. The shape factor f is calculated as[16]:

$$f = \frac{4\pi A}{L^2} \quad (1)$$

where f ranges from 0 to 1, with values closer to 1 indicating a more spherical morphology. As shown in Fig. 5(b), the f value increases from 0.067 for K0 to 0.353 for K2, confirming the effectiveness of K_2SO_4 modification in promoting M_2B spheroidization.

Surface-active elements can segregate at the interface of eutectic phases (e.g., borides or carbides), inhibiting their growth. EPMA mapping confirms K enrichment at specific locations (Points 1 and 2 in Fig. 6) along the boundary between M_2B and the matrix. K is not detected within the M_2B or the matrix itself. This indicates that during solidification, K enriches in the diffusion layer ahead of the M_2B/melt solid-liquid interface[17], forming an adsorbed film (i.e., K-rich layer). This film impedes the diffusion of C, Fe, and Cr atoms into M_2B, reducing its growth rate and promoting a more spherical or blocky morphology.

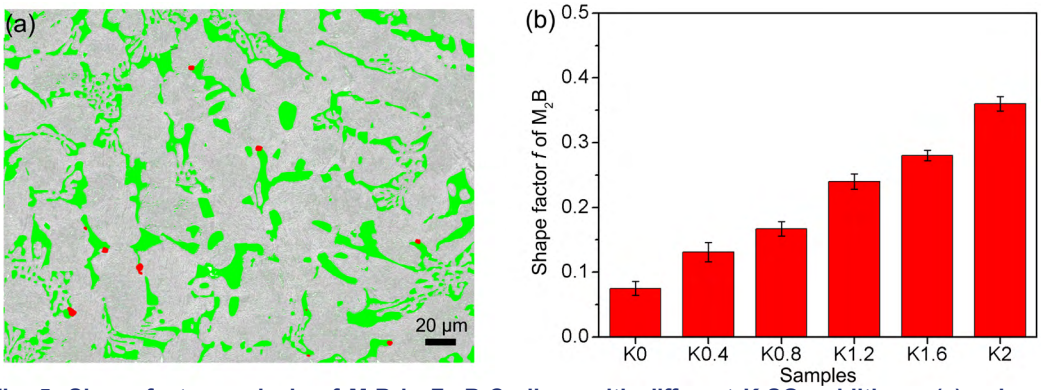

Fig. 5: Shape factor analysis of M_2B in Fe-B-C alloys with different K_2SO_4 additions: (a) colored image exemplified by the K2 sample; (b) shape factor f value

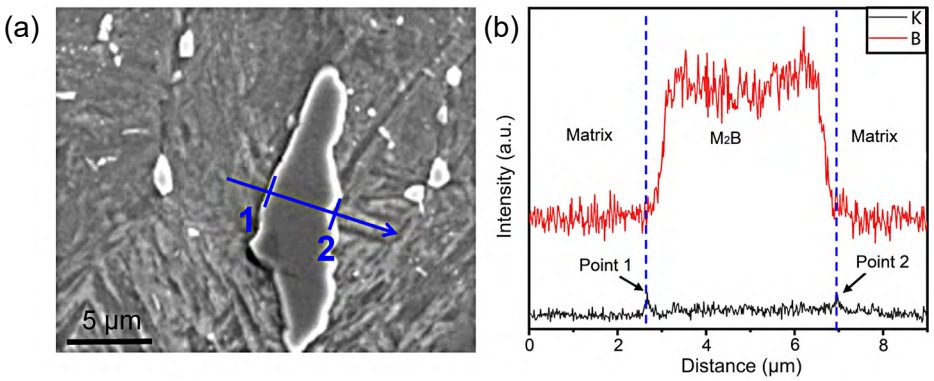

Fig. 6: Distribution of K in the K2 sample: (a) SEM micrograph; (b) EPMA line scan profile

3.2 Mechanical properties

Figure 7 shows the macrohardness and impact toughness of Fe-B-C alloys with different K_2SO_4 additions. Hardness increases slightly with K_2SO_4 addition, reaching a maximum of 61.42 HRC for the K2 sample (4.46wt.% K_2SO_4), as shown in Fig. 7(a). This is attributed to the formation of MnS and the increase of $M_{23}(B,C)_6$ phase, as shown in Fig. 2. Toughness increases progressively from 5.9 $J\cdot cm^{-2}$ to 14.2 $J\cdot cm^{-2}$ with K_2SO_4 addition, reaching a maximum for the K2 sample, as shown in Fig. 7(b). This improvement is primarily due to the modified M_2B morphology. In the K0 sample, the three-dimensional boride network disrupts matrix continuity[18], leading to high stress concentration and easier crack propagation along the brittle M_2B network. In the K2 sample, the isolated blocky M_2B significantly improves the continuity of the α-Fe matrix, enhancing the impact toughness.

The fracture surfaces after impact testing for the K0, K1.2, and K2 samples are shown in Fig. 8. The K0 sample exhibits a cleavage-dominated fracture surface with characteristic features of intergranular brittle failure. The continuous boride network constrains both α-Fe and M_2B, preventing plastic deformation and resulting in a brittle fracture surface[19]. Fracture surfaces of the K1.2 and K2 samples show smooth cleavage facets alongside ductile dimples, with the K2 sample exhibiting more dimples than the K1.2 sample. This indicates a transition from brittle fracture to a ductile-cleavage mixed fracture mode, facilitated by the spheroidization and fragmentation of the boride network and the consequent increase in the matrix continuity.

3.3 Three-body abrasion

Figure 9 shows the three-body wear weight loss of the Fe-B-C alloys and Cr26 high-chromium cast iron under three different load conditions: 10 N, 30 N, and 50 N. With the increase of K_2SO_4 addition in the alloy, the wear weight loss decreases gradually, indicating that the addition of K_2SO_4 has a significant positive effect on improving the three-body wear resistance of the Fe-B-C alloy. A comparison with Cr26 high-chromium cast iron reveals that under the different load conditions, the three-body wear weight loss of the K2 alloy is lower than that of Cr26. This reflects that under the same load, the wear resistance of the K2 alloy is overall better than that of Cr26, demonstrating that the modified Fe-B-C alloy has broader application potential in three-body wear working conditions.

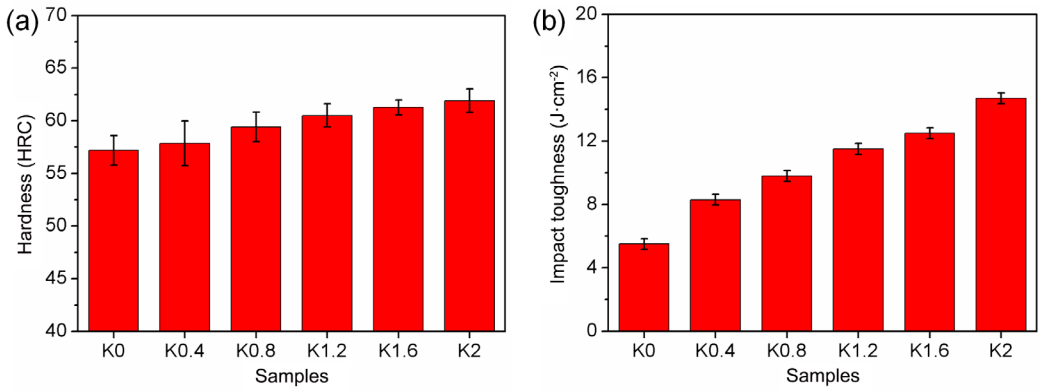

Fig. 7: Macrohardness (a) and impact toughness (b) of Fe-B-C alloys with different K_2SO_4 additions

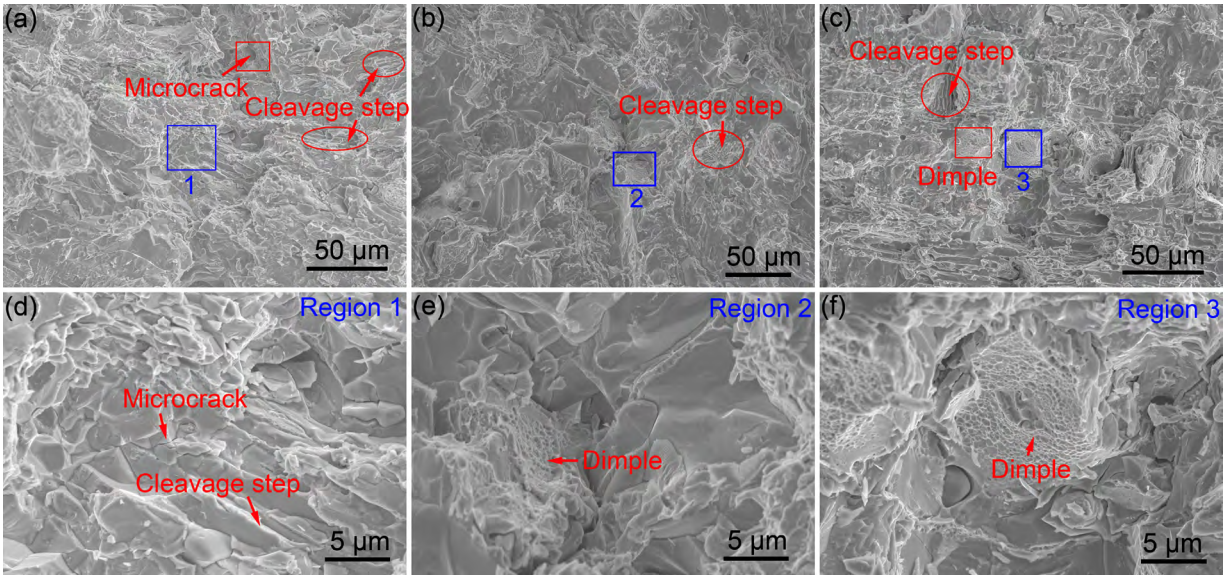

Fig. 8: SEM images of impact fracture surfaces: (a, d) K0; (b, e) K1.2; (c, f) K2; (d, e, f) magnified views of regions in images (a), (b), and (c), respectively

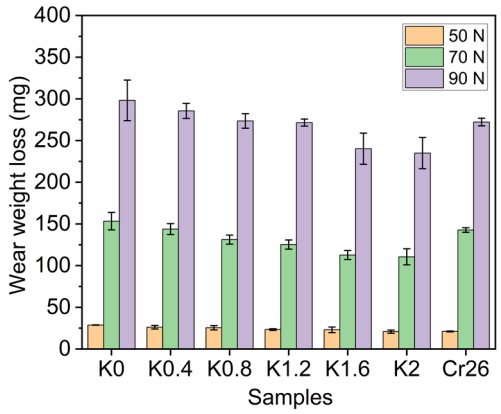

Fig. 9: Three-body abrasion weight loss of Fe-B-C alloys under different loads

SEM morphologies of the wear tracks under the load of 50 N are shown in Fig. 10. During three-body abrasion, the surface undergoes repeated rolling and grinding by the WC particles, resulting in features like fatigue spalling, fragmentation, and micro-grooves. The K0 sample shows a rough surface with grooves and spalling. From the K0.4 sample to the K1.6 sample, the wear track surfaces become progressively smoother, with reduced spalling. The K2 sample exhibits significantly reduced spalling.

3D topographies of the wear tracks under the load of 50 N are shown in Fig. 11. Due to the fracture and spalling of M_2B, raised humps (marked by red circles) and pits (marked by blue rectangles) are visible on the wear surfaces. The K0 sample exhibits numerous large humps and pits on its wear track surface with high surface roughness. As the K_2SO_4 addition increases, the size and number of humps and pits decrease significantly. The K2 sample shows minimal peak-like humps and pits. These demonstrate that the K_2SO_4 modification substantially reduces the wear weight loss and surface damage of the Fe-B-C alloy.

Figure 12 shows the SEM morphologies of the wear subsurface of Fe-B-C alloys with different K_2SO_4 additions under the load of 50 N. In the K0 and K0.4 samples, debris embedded in the alloy matrix can be observed, indicating that the M_2B is crushed into fragments during the wear process.

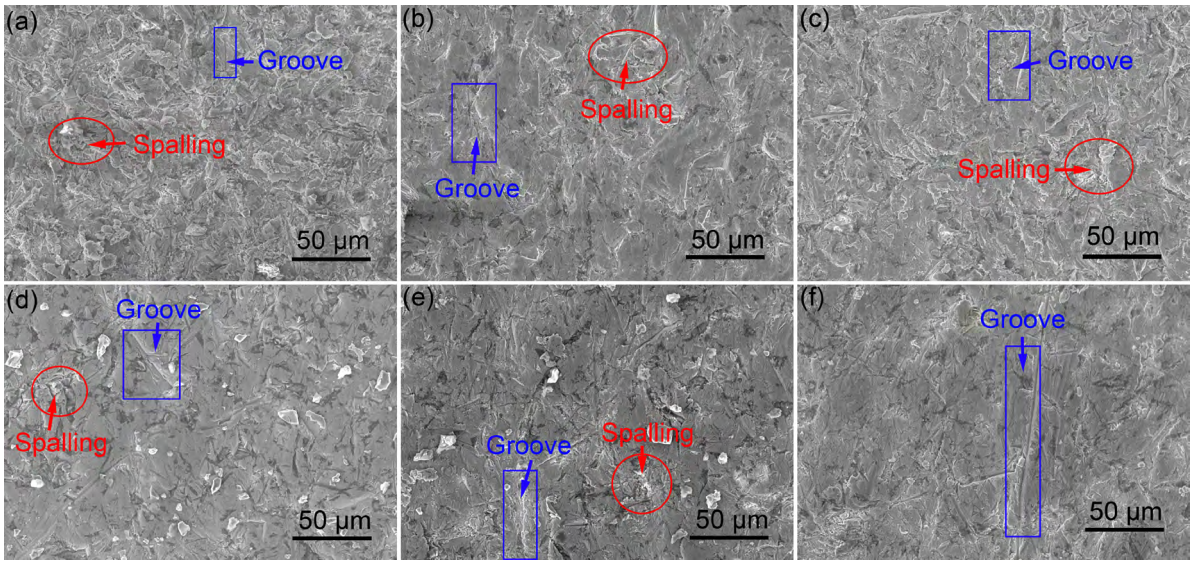

Fig. 10: SEM images of wear tracks under 50 N: (a) K0; (b) K0.4; (c) K0.8; (d) K1.2; (e) K1.6; (f) K2

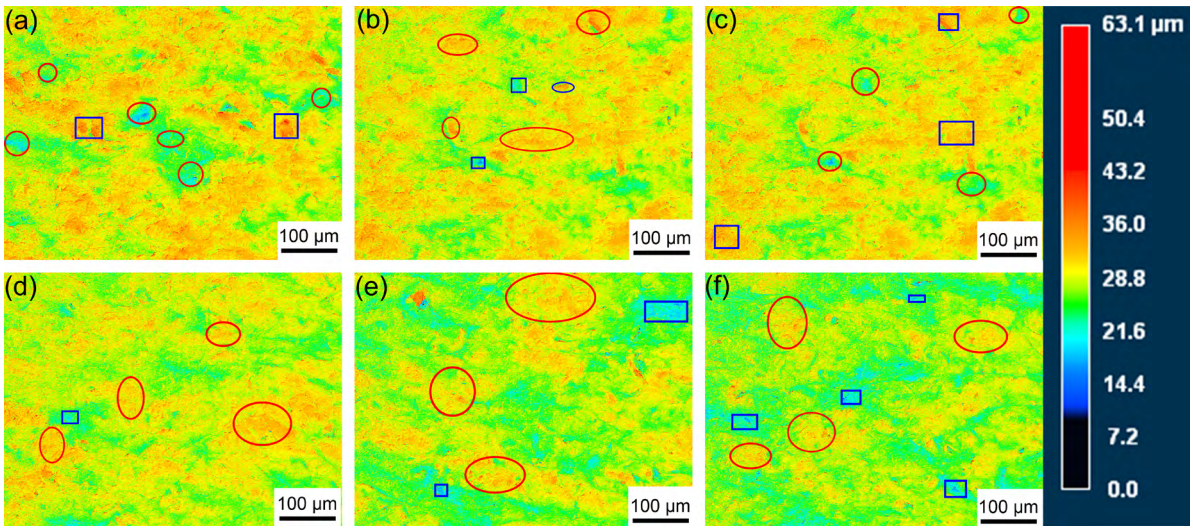

Fig. 11: 3D topographies of wear tracks under 50 N: (a) K0; (b) K0.4; (c) K0.8; (d) K1.2; (e) K1.6; (f) K2

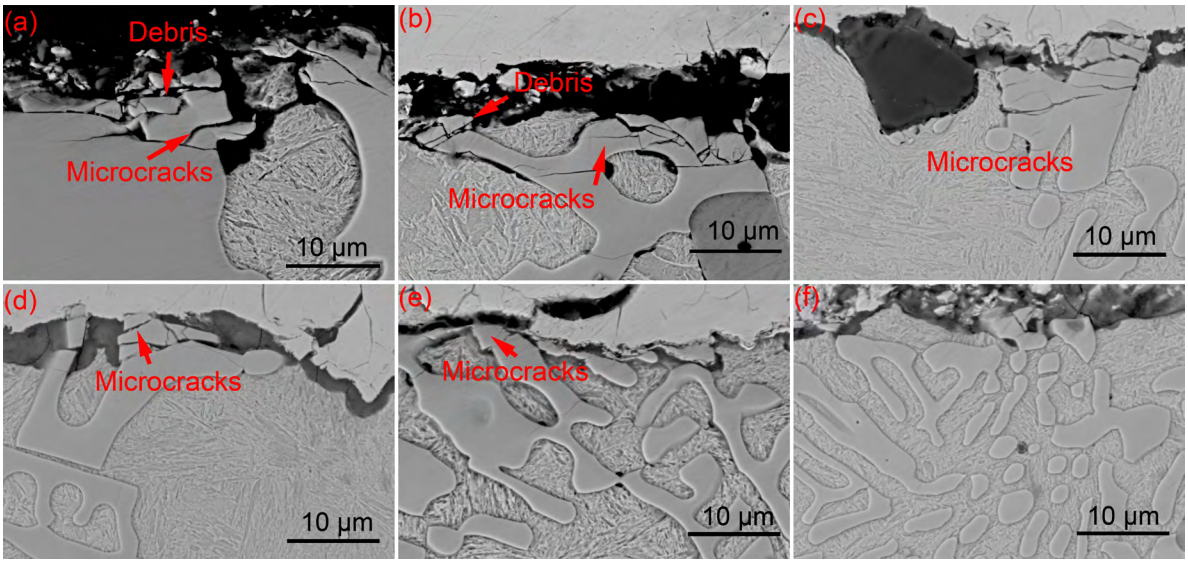

Fig. 12: Worn subsurface SEM images of Fe-B-C alloys with different K_2SO_4 additions under 50 N: (a) K0; (b) K0.4; (c) K0.8; (d) K1.2; (e) K1.6; (f) K2

Additionally, numerous microcracks are visible within the M_2B. This occurs because the thin network-shaped M_2B cannot provide sufficient resistance against wear by the WC particles during three-body abrasion. The thin network-shaped M_2B is slid over, fractured, and then plowed up by the large WC abrasives, resulting in a relatively rough wear morphology. With the addition of K_2SO_4, the microcracks decrease gradually, and debris becomes almost invisible, as can be seen in Figs. 12(c, d). In the K1.6 and K2 samples, microcracks are scarcely observed. This is attributed to the addition of K_2SO_4, which promotes the spheroidization of the M_2B network, transforming it into the isolated block-like structure. This spheroidized and isolated M_2B phase inhibits the initiation and propagation of microcracks caused by fatigue wear, thereby effectively protecting the matrix from wear during three-body abrasion.

4 Conclusions

(1) The Fe-B-C alloy primarily consists of α-Fe and M_2B phases. Adding K_2SO_4 leads to the formation of a new phase of α-MnS, and the K element enriches at the boundary between the M_2B phase and the matrix, which thereby promotes the structure transformation of the M_2B phase from continuous network to isolated blocky.

(2) With increasing K_2SO_4 addition, the hardness of the Fe-B-C alloy increases from 56.37 HRC to 61.42 HRC, and the impact toughness increases from 5.9 $J·cm^{-2}$ to 14.2 $J·cm^{-2}$. The fracture mode transitions from cleavage fracture to a ductile-cleavage mixed fracture.

(3) Three-body abrasion weight loss of the Fe-B-C alloy decreases and gradually stabilizes as the K_2SO_4 addition increases, with the alloy containing 4.46wt.% K_2SO_4 exhibiting the best wear resistance. The blocky M_2B phase effectively resists abrasion and suppresses the initiation and propagation of microcracks during wear.

Acknowledgments

This work was financially supported by the Natural Science Foundation of Guizhou Province (Grant No.: Qiankehe Foundation-ZK[2024] General 522), the Doctoral Research Start-up Fund of Guiyang University (Grant No.: GYU-KY-[2025]), the Young Talents Cultivation Program Project of Guangdong Association for Science and Technology (Grant No.: SKXRC2025059), and the Fundamental Research Funds for the Central Universities (Grant No.: 21625404).

Conflict of interest

The authors declare that they have no known competing financial interests or personal relationships that could have appeared to influence the work reported in this paper.

References

[1] Jian Y, Ning H, Huang Z, et al. Three-body abrasive wear behaviors and mechanism analysis of Fe-B-C cast alloys with various Mn contents. Journal of Materials Research and Technology, 2021, 14: 1301–1311.
[2] Tian Y, Fu H G. Development of Fe-Cr-B wear-resistant alloys. China Foundry Machinery & Technology, 2018, 53(3): 5–11. (In Chinese)
[3] Fu H, Jiang Z. A study of abrasion resistance cast Fe-B-C alloy. Acta Metallurgica Sinica, 2006, 42(5): 545–548.
[4] Song S, Yi Y, Xing J, et al. Microstructure evolution, crystallography, nanomechanical properties and wear-resistance of multi-component M_2B in Fe-B alloy. Journal of Materials Research, 2022, 37: 1429–1439.
[5] Ma S, Xing J, He Y, et al. Effect of orientation and lamellar spacing of Fe_2B on interfaces and corrosion behavior of Fe-B alloy in hot-dip galvanization. Acta Materialia, 2016, 115: 392–402.
[6] Ma S, Xing J, Fu H, et al. Microstructure and crystallography of borides and secondary precipitation in 18 wt.% Cr-4 wt.% Ni-1 wt.% Mo-3.5 wt.% B-0.27 wt.% C steel. Acta Materialia, 2012, 60(3): 831–843.

[7] Yi D, Xing J, Ma S, et al. Investigations on microstructures and two-body abrasive wear behavior of Fe-B cast alloy. Tribology Letters, 2012, 45: 427–435.
[8] Zhang J, Liu J, Liao H, et al. A review on relationship between morphology of boride of Fe-B alloys and the wear/corrosion resistant properties and mechanisms. Journal of Materials Research and Technology, 2019, 8(6): 6308–6320.
[9] Guo B, Wang H, Song G, et al. Co/Co_2P heterojunction embedded in N, P and S co-doped carbon nanocages for enhancing polysulfide conversion in lithium sulfur batteries. Journal of Colloid and Interface Science, 2025, 699: 138133.
[10] Yu B, Fei L, Li M, et al. Ultrathin lithium metal anodes for high-efficiency lithium batteries: Synergizing surface LiF and lithiophilic alloying. Energy Storage Materials, 2025, 82: 104579.
[11] Liu H, Fu P, Liu H, et al. Effects of rare earth elements on microstructure evolution and mechanical properties of 718H pre-hardened mold steel. Journal of Materials Science & Technology, 2020, 50: 245–256.
[12] Yu B, Fei L, Chen L, et al. MoP/MoO_2 nanodot heterostructures supported on N, P-Doped carbon nanotube metworks as scalable and efficient electrocatalysts for oxygen evolution reaction. Journal of Alloys and Compounds, 2025, 1029: 180729.
[13] Sare I R. Abrasion resistance and fracture toughness of white cast irons. Metals Technology, 1979, 6(1): 412–419.
[14] Li Q, Chen Y, Huang X, et al. Long-whisker type TiB phase introduced by micron-sized precursors and its prominent strengthening effect in titanium matrix composites. Materials Science and Engineering: A, 2022, 841: 143021.
[15] Li Q, Yi Y, Zhao Y, et al. Two-body and three-body abrasive wear behaviors of Fe-2wt%B alloy modified with various K_2SO_4 additions. Tribology Transactions, 2023, 66(4): 733–745.
[16] Yi Y, Li Q, Huang X, et al. Influence mechanism of K_2SO_4 addition on microstructure, mechanical properties and abrasion resistance of Fe-2wt%B alloy. Materials & Design, 2021, 197: 109164.
[17] Ownby P D, Liu J. Surface energy of liquid copper and single-crystal sapphire and the wetting behavior of copper on sapphire. Journal of Adhesion Science and Technology, 1988, 2(1): 255–269.
[18] Yi Y, Xing J, Lu Y, et al. Investigations on microstructure, mechanical properties and abrasion resistance of 4wt%Cr-2wt%Mn-2wt%Cu-Fe-B alloy. Materials Characterization, 2018, 137: 222–230.
[19] Yi Y, Xing J, Lu Y, et al. Effect of normal load on two-body abrasive wear of an Fe-B-Cr-C based alloy with minor Cu and Ni additions. Wear, 2018, 408: 160–170.